Evolution of nano-pores during annealing of technically pure molybdenum sheet produced from different sintered formats

International Journal of Refractory Metals and Hard Materials 110 (2023) 106032

Contents lists available at ScienceDirect

International Journal of Refractory Metals and Hard Materials

journal homepage: www.elsevier.com/locate/IJRMHM

Evolution of nano-pores during annealing of technically pure molybdenum sheet produced from different sintered formats

S. Jakob [a,b], A. Lorich [c], W. Knabl [c], A. Stark [d], P. Staron [d], H. Clemens [a], P. Spoerk-Erdely [a], V. Maier-Kiener [a,*]

[a] Department of Materials Science, Montanuniversität Leoben, Franz-Josef-Str. 18, 8700 Leoben, Austria
[b] Now at: Department of Physics, Chalmers University of Technology, 412 96 Göteborg, Sweden
[c] Plansee SE, Metallwerk-Plansee-Str. 71,6600 Reutte, Austria
[d] Institute of Materials Physics, Helmholtz-Zentrum Hereon, Max-Planck-Straße 1, 21502 Geesthacht, Germany

ARTICLE INFO

Keywords:
Molybdenum
Porosity
Recrystallization
SAXS
Synchrotron
Volatilization

ABSTRACT

Molybdenum is a refractory metal with no phase transformation in the solid state and a high melting point. It is therefore an excellent structural material for various high temperature applications. Especially in this field of operation, significant creep resistance is essential. To achieve this, a microstructure with grains in the range of millimeters is desired. However, as demonstrated in the present study, the onset temperature for secondary recrystallization, which would lead to a beneficial grain size, is among other things dependent on the initial dimensions of the sintered part. One possible reason for the different microstructural evolutions is the influence of residual pores in sub-micrometer size. Sheets were thus fabricated via three different production routes employing the same initial Mo powder to exclude chemical variation as an influencing factor. The samples were investigated by in-situ small-angle X-ray scattering at a synchrotron radiation source with two different heating rates. Additionally, selected annealed samples were studied ex-situ with high energy X-rays. The apparent volume fraction of pores is compared to a volatilization model for the vaporization of typical accompanying elements and the induced thermal expansion.

1. Introduction

Mo is part of the group of refractory metals and has a body-centered cubic lattice structure and a high melting point of 2620 °C. It experiences no phase transformation during heating in the solid state and maintains its mechanical strength up to elevated temperatures. Beside mechanical properties, the good electrical and thermal conductivity as well as a low coefficient of thermal expansion offer applications in electronics, coatings or high performance lighting technology [1]. In various high-temperature applications, such as medical technology or furnace equipment, Mo cannot be replaced due to physical or economic reasons. In these instances, creep resistance is one of the crucial material properties.

In order to optimize the creep behavior, the knowledge of the recrystallization behavior is of paramount importance [2]. Especially the understanding of the so-called secondary recrystallization process and the associated grain growth is essential [3–5]. A low onset temperature for secondary recrystallization, e.g. around 1700 °C, is desired for creating sufficiently coarse-grained microstructures to ensure low creep rates.

Because of its high melting point, technically pure Mo is mainly produced by powder metallurgy. To improve certain material properties and to increase the production yield, a transition to larger sintered formats as starting material is required. However, preliminary microstructural investigations by the authors have shown that in the desired larger sintered formats the onset of secondary recrystallization is shifted to significantly higher temperatures of approximately 2200 °C. In some cases no grain growth occurs at all and the microstructure remains unfavorably fine-grained. Since the development of non-sag W with K dopant for lighting bulb wires, it is known that pores can behave like particles in regard to the mobility of grain boundaries [6–8]. It is therefore assumed that one of the critical influences for the diverging behavior in secondary recrystallization of Mo may be the porosity and especially sub-micron pores within the rolled sheet material.

This study aims at distinguishing the differences in pore content and evolution concerning the different dimensions of the initial sintered

* Corresponding author.
E-mail address: verena.maier-kiener@unileoben.ac.at (V. Maier-Kiener).

https://doi.org/10.1016/j.ijrmhm.2022.106032
Received 25 May 2022; Received in revised form 10 October 2022; Accepted 17 October 2022
Available online 20 October 2022

parts. The same starting powder is processed to deter any influence of chemical variation of the pre-material. Small-angle X-ray scattering (SAXS) with high-energy synchrotron radiation is used to analyze pores in the size regime of several nanometers. The obtained evolution of pore volume is compared to the result of a simple volatilization model for impurity elements.

2. Materials and methods

The Mo sheets were powder-metallurgically produced by Plansee SE (Reutte, Austria) from the same initial powder. Three different production routes were chosen:

i) The pre-material for the first sheet sample, labelled as **Mo1**, was a small sintered part.
ii) For the second sample, termed **Mo2**, a pre-material plate machined from a large sintered part to the same dimensions as in Mo1 was used.
iii) Third, the remaining part of the large sintered format was processed to sheet dimensions and the resulting sample is denoted by **Mo3**.

Samples of Mo3 were recrystallized once before final rolling was performed in the same manner as for all three variants to achieve sheet material with 1 mm thickness. Fig. 1 shows the initial microstructures in the longitudinal cross-section investigated by electron backscatter diffraction (EBSD). Chemical analysis of the three sheet samples was performed and the contents of accompanying elements are depicted in Table 1. Two measurements were conducted and either the average value or the result of both measurements are displayed. The analysis shows a typical chemical composition for technically pure Mo sheet with some variation in the C and O content and only slight differences in the H, K and Fe content between the three variants. Microstructural investigations have been performed as well as density measurements of work-hardened (WH) and annealed samples by weight balance (buoyancy method) according to ISO 3369 [9]. Samples with dimensions of $10 \times 5 \times 1$ mm^3 were cut with the long axis aligned in the rolling direction for the investigation at the synchrotron facility.

The SAXS experiments were conducted at the P07 high-energy materials science (HEMS) beamline operated by the Helmholtz-Zentrum Hereon at PETRA III at the Deutsches Elektronen-Synchrotron (DESY), Germany. Using a modified quenching and deformation dilatometer DIL805A/D [10] by TA Instruments, Germany, the samples were heated under vacuum atmosphere with two different temperature profiles. Some samples were heated from room temperature (RT) to 760 °C with 300 K/min before using a constant rate of 1 K/min between 760 °C and 1500 °C. Another set of samples was heated with a constant heating rate of 1000 K/min from RT to 1500 °C, followed by a holding time of 5 min. The temperature was measured by means of type S thermocouples spot-welded onto the specimens. To analyze the development of the scattering signal for higher temperature ranges, additional samples were heated with a rate of about 100 K/min and annealed at either 1500 °C, 1700 °C, 1900 °C, 2100 °C or 2400 °C for 1 h under H_2 atmosphere prior to the beamtime. These samples were then exposed to the synchrotron X-rays in an ex-situ manner. Regarding the incident X-ray beam, a mean photon energy of 103 keV ($\lambda = 0.1204$ Å) was selected. A Perkin Elmer (PE) XRD 1621 flat panel detector with a pixel matrix of 2048 × 2048 and a pixel size of 200 × 200 µm^2 was used. The PE detector was placed at a distance of 10,078 mm from the specimens (calibrated with a standard silver behenate sample), and a beam stop made of crossed W sheets with a thickness of 0.2 mm and a length of 1 mm was used. The cross-section of the incident beam was set to 0.18 × 0.18 mm^2. This setup was calibrated using a glassy carbon standard. SAXS patterns were recorded continuously during the heating experiments with an exposure time of 30 s for the heating rate of 1 K/min and 1 s for 1000 K/min. The exposure time for the ex-situ annealed samples was set to 30 s. For the further data evaluation, the 2D patterns were corrected for background scattering, electronic noise and transmission. The detector images were azimuthally integrated with the aid of the software package Fit2D [11]. The length of the scattering vector is given by $|q| = q = 4\pi/\lambda \bullet \sin\theta$, where 2θ represents the Bragg angle of the scattered photons. The scattering curves were fitted with a lognormal size distribution of scattering centers over a scattering vector q range of 0.08 to 0.5 nm^{-1} using the program SANSFit, which is based on a least-squares procedure as described in [12]. The scattering contrast $\Delta\eta$, which represents the difference in the scattering length densities of the matrix and the pores,

Table 1
Concentrations of accompanying elements in Mo sheet samples; a…carrier-gas analyses, b…inductively coupled plasma – mass spectrometry, c…combustion analyses, d…graphite tube – atomic adsorption spectrometry. Contents denoted with '<' are below the detection limit of the analyzing method.

Element [µg/g]	Mo1	Mo2	Mo3
H[a]	< 1	< 1 / 2	< 1
B[b]	< 2		
C[c]	< 5 / 8	<5	8
N[a]	< 5		
O[a]	6	12	12
Na[b]	< 5		
Mg[b]	< 5		
Al[b]	< 1		
Si[d]	6		
P[b]	2		
S[c]	< 5		
K[b]	4	5	5
Ca[b]	< 2		
Ti[b]	1		
Cr[b]	2		
Fe[b]	6	5	5
Hf[b]	1		
W[b]	180	174	175

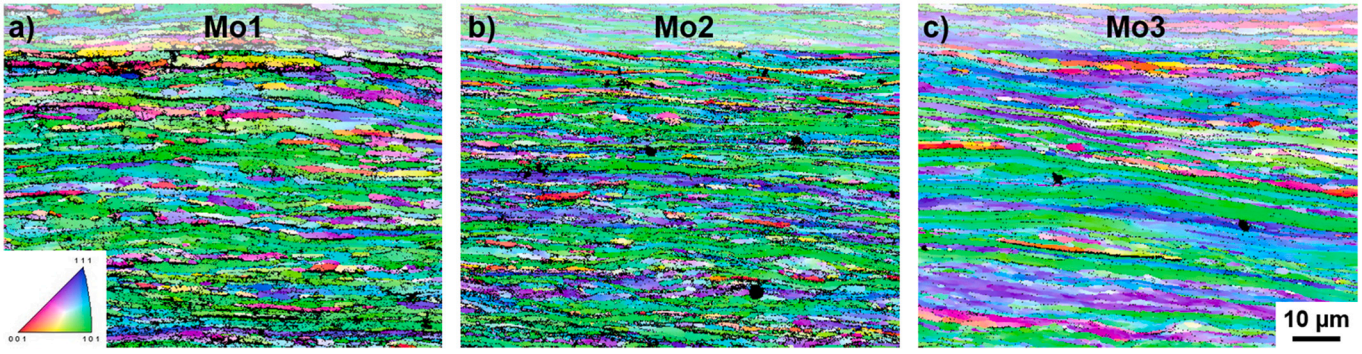

Fig. 1. ESBD micrographs of the initial microstructures in longitudinal cross-section. Points that could not be indexed are depicted in black.

was set to the constant value of 7.62×10^{11} cm^{-2}. The integration of the macroscopic differential scattering cross-section dΣ/dΩ according to

$$Q = 4\pi \int_0^{\infty} \frac{d\Sigma}{d\Omega}(q) q^2 \mathrm{d}q \quad (1)$$

yields the integrated intensity Q, which is proportional to the product of the scattering contrast Δη and the volume fraction f of the scattering centers. In this paper, the observed intensities were likewise integrated over a limited q-range of 0.08 to 0.5 nm^{-1}. Therefore, the resulting integrated intensity, which was termed Q', gives a more qualitative comparison of the scattering centers.

3. Results

Prior to the synchrotron measurements, samples of all three production routes were annealed at high temperatures ranging from 1500 °C to 2400 °C to assess the propensity for secondary recrystallization. Fig. 2 shows light-optical micrographs of the microstructures after annealing for 1 h in H_2 atmosphere. Mo1 shows the strongest tendency to develop large grains. The onset temperature for secondary recrystallization is already below 1700 °C. Mo2 shows a limited driving force for grain growth and is predominantly coarse-grained at 1900 °C. Mo3 has the strongest retardation for secondary recrystallization and remains fine-grained up to 2400 °C. Only at 1900 °C are a few coarse

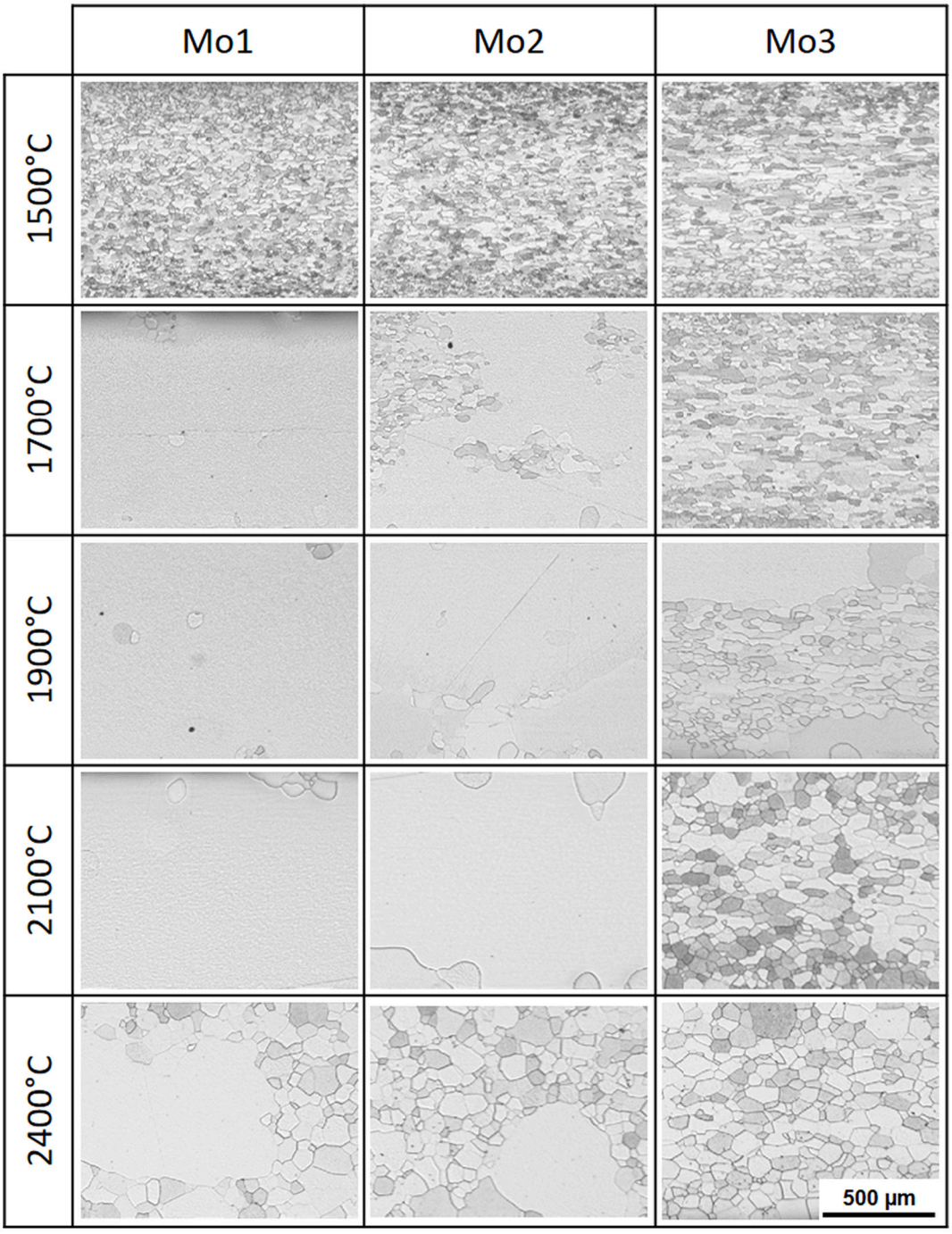

Fig. 2. Light-optical micrographs of the microstructures of the three different sample variants annealed in H_2 atmosphere to the indicated temperatures. The heating rate was about 100 K/min and the holding time at annealing temperature was 1 h.

grains visible at the surface of the sample. Interestingly, Mo1 and Mo2 have a partly fine-grained microstructure at the highest annealing temperature of 2400 °C.

SAXS data was collected at the synchrotron facility from samples ex-situ annealed as represented in Fig. 2. Additionally, sheet samples of all three production routes were in-situ heated. From the scattering data, volume fractions as well as the mean radii of the pore size distributions were fitted. The results are depicted in Figs. 3-5.

Fig. 3 shows the results of the in-situ experiments with 1 K/min heating rate. All three sample variants display a trend towards increased volume fraction of scattering centers, e.g. pores, with increasing temperature. Mo1 (Fig. 3a) depicts a further increase at 1000 °C. The mean

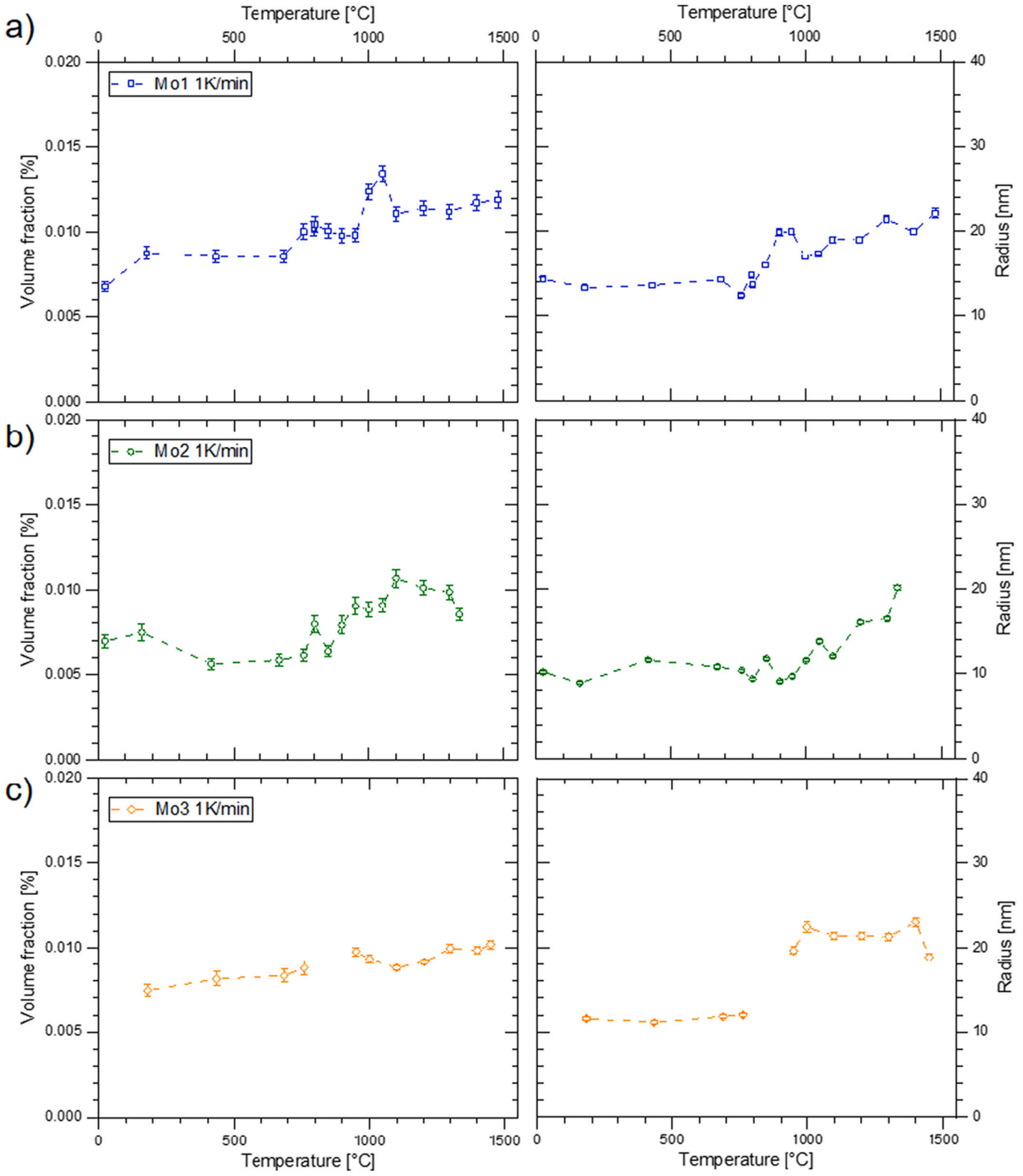

Fig. 3. Fitted volume fraction and mean radius of azimuthally averaged scattering data of the in-situ 1 K/min heating experiments (see text).

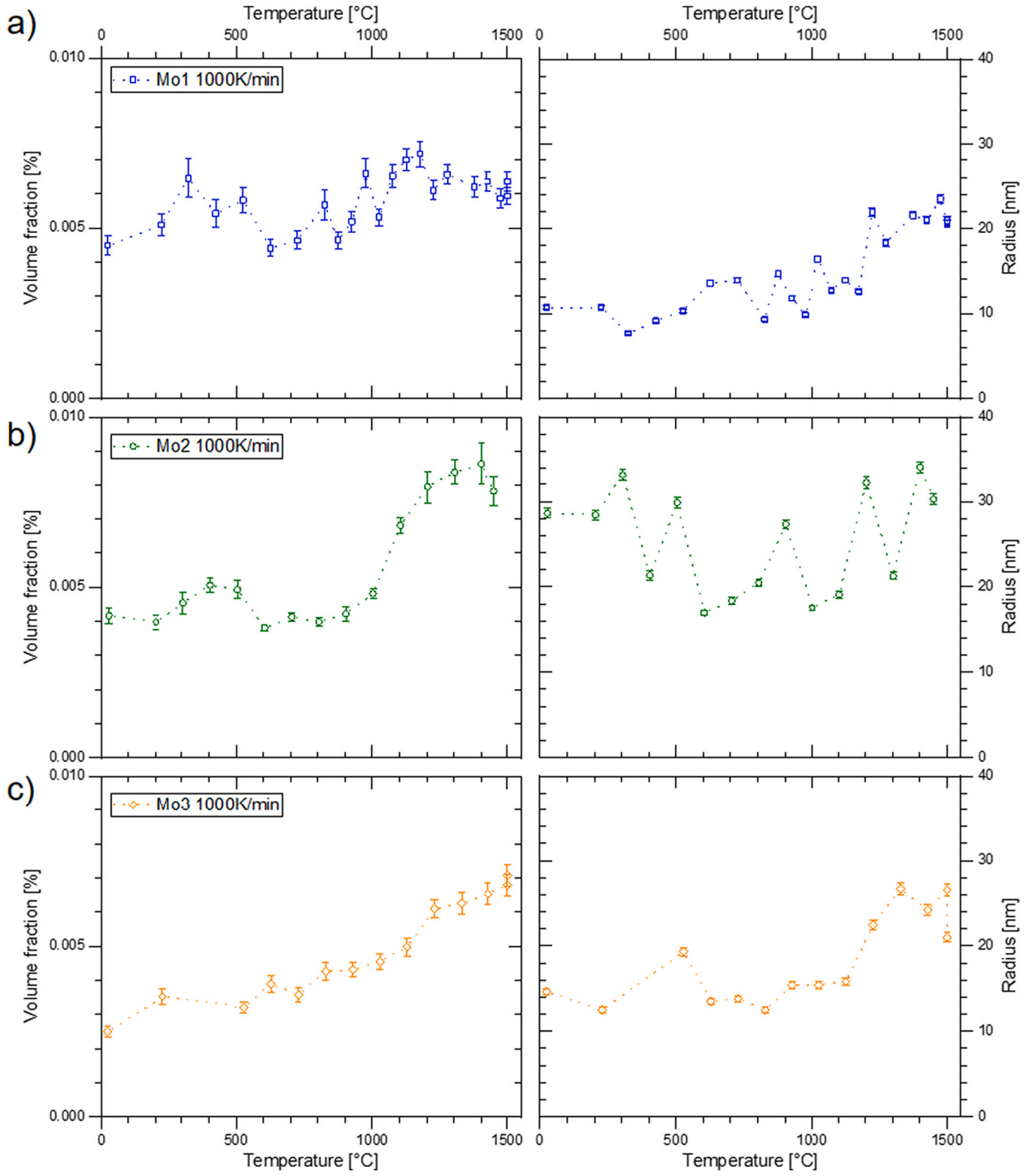

Fig. 4. Fitted volume fraction and mean radius of azimuthally averaged scattering data of the in-situ 1000 K/min heating experiments. See text for details.

radius shows values increasing from 12 nm to about 22 nm, with the growth process starting at 900 °C. Mo2 does not display such a distinct increase in volume fraction. However, an increase is observed between 1050 and 1100 °C (Fig. 3b). The mean radius of pores remains at about 10 nm up to 1000 °C, followed by an increase to 20 nm at 1330 °C. The experiment was aborted at this temperature because of a detached thermocouple. Several points in the Mo3 curves were excluded due to a beam loss of the synchrotron and subsequent intensity variations. The volume fractions between 950 and 1450 °C are therefore normalized to the last valid point at 760 °C (Fig. 3c). The mean radii remain at about 12 nm between RT and 760 °C. At higher temperatures the mean pore size increased up to 24 nm.

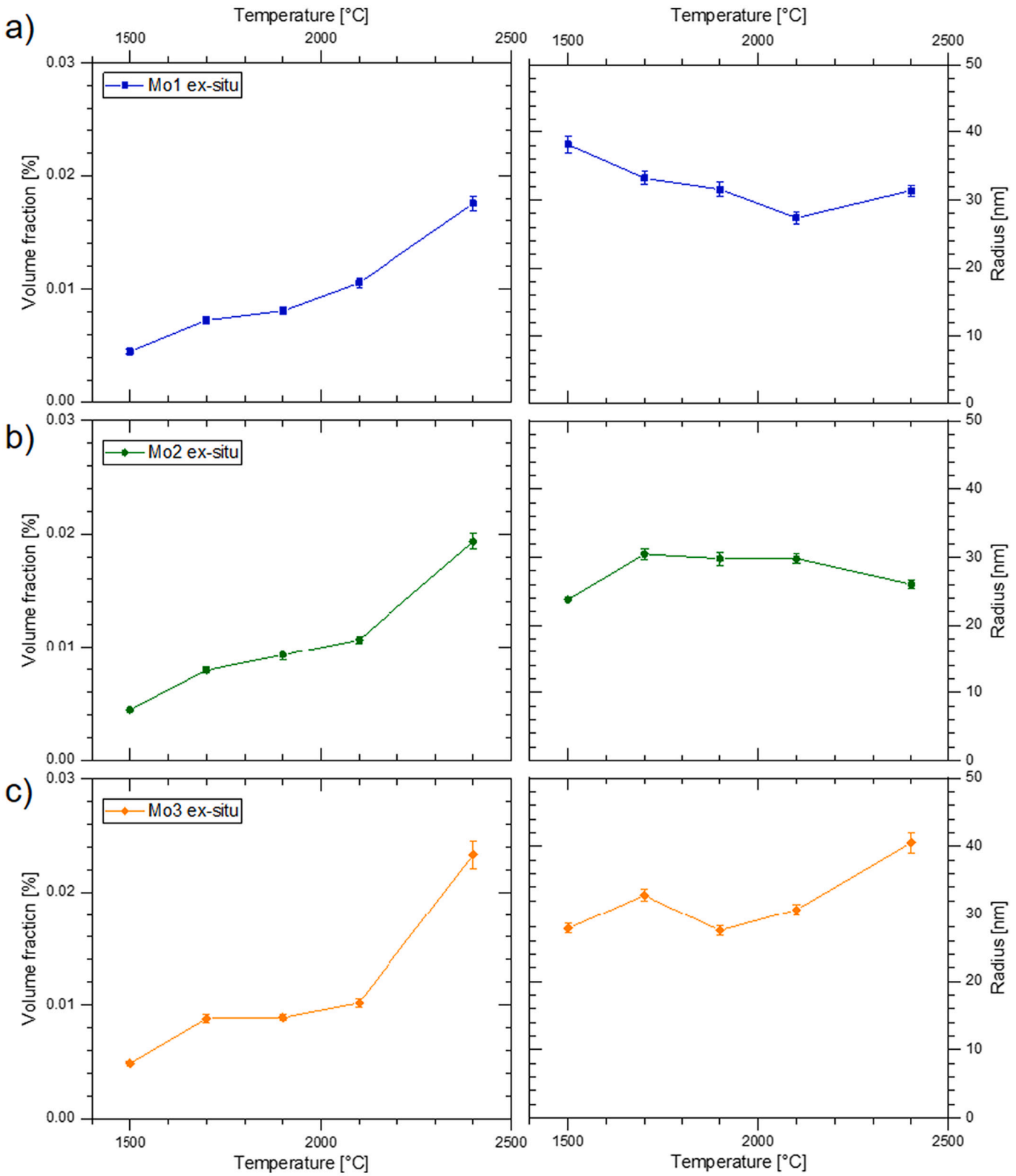

Fig. 5. Fitted volume fraction and mean radius of azimuthally averaged scattering data of the ex-situ annealed samples (see text).

Experiments with 1000 K/min heating rate are depicted in Fig. 4. The volume fraction of pores shows a slight increase for Mo1 with increasing mean radii size (Fig. 4a). The run of the Mo2 sample, as can be seen in Fig. 4b, shows a distinct increase in pore volume fraction at about 1100 °C. The size of the mean radii of the pores remains slightly smaller than 30 nm. The fitted volume fraction in Mo3 displays a continuous increase with further rise at 1200 °C. The mean pore size increases from 15 nm to about 25 nm (Fig. 4c).

Figs. 5a to c show the fitted volume fractions as well as the mean pore radii of the ex-situ annealed samples. Interestingly, for all three series the volume fraction shows a similar trend. A first increase in pore content is visible between 1500 °C and 1700 °C. Afterwards, the volume

fraction raises only slightly up to 2100 °C. At the highest annealing temperature of 2400 °C, another drastic increase in volume fraction is visible. This is most pronounced for sample Mo3 (Fig. 5c) and least observed for the Mo1 variant (Fig. 5a). The mean radii of the fitted pore size distributions vary between 25 nm and 40 nm.

As a complementary method, density measurements were performed using the buoyancy method. Beside the investigation of samples in the WH and annealed state (2400 °C), measurements of the same samples before and after heat treatment were performed to gain direct information. Fig. 6 shows the densities of samples from all three variants before and after annealing. All WH samples exhibit relative densities above 99%. Mo3 has the highest density of the variants. After annealing to 2400 °C with 1 h holding time, the average densities have decreased. While the reduction is not significant for Mo1, Mo2 shows a reduction of 0.033 g/cm^3, whereas Mo3 exhibits the strongest decrease of 0.087 g/cm^3 or 0.85% of the relative density.

Samples were annealed at 2100 °C and 2400 °C for 1 h. Bending of the specimens at RT leads to brittle fracture. Fig. 7 shows scanning electron microscopy (SEM) images of the corresponding fracture surfaces. Mo1 and Mo2 samples annealed to 2100 °C show transgranular fracture mode, since the samples have a coarse-grained microstructure (see Fig. 2). Only a few isolated pores are visible. The fractograph in Fig. 7c shows a number of small pores at the grain boundaries of Mo3 that fractured partly in an intercrystalline way. Figs. 7d to f show the fracture surfaces of the samples annealed to 2400 °C. Mo1 shows a mostly coarse-grained microstructure with only a small proportion of intercrystalline fracture. Pores with diameters up to 1 µm are present at these grain boundaries. However, pores are also visible within the grains, as can be seen in the area of transcrystalline fracture of the sample. Mo2 and Mo3 show mixed fracture mode and predominately a fine-grained microstructure. Again, the grain boundaries are covered with µm-sized pores. From the fractographs, a distinct difference in the amount of pores is visible between the different annealing temperatures for all sample variants.

4. Discussion

In order to eliminate some potential influences causing the observed different secondary recrystallization behavior, the samples in this study were produced from the same initial Mo powder. Any difference in chemical composition should, therefore, stem from the different production route for small or large sintered parts and to a lesser extent from the thermo-mechanical procedure afterwards. The parameters of the rolling process were kept as equal as possible. Only for Mo3, a preceding step was necessary as this variant had a greater thickness after sintering.

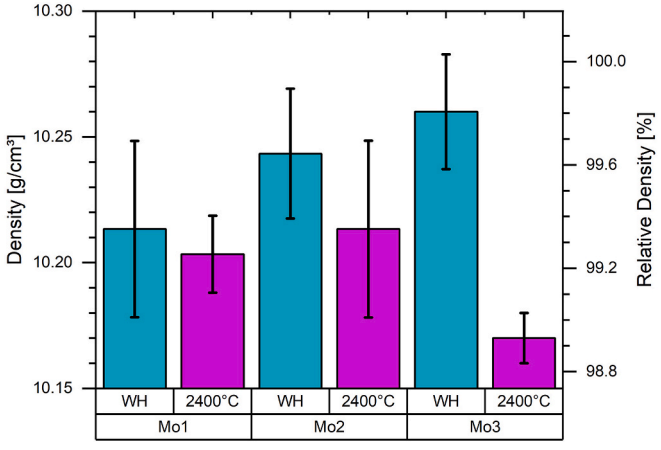

Fig. 6. Density measurements (buoyancy method) of three samples each before and after annealing to 2400 °C for 1 h in H_2 atmosphere with a heating rate of about 100 K/min.

Thus, Mo3 was primary rolled to the same dimension as Mo1 and Mo2 in the as-sintered state and then heat-treated to recrystallize the microstructure. Starting from this point, the rolling sequence was the same for all three sample variants to achieve sheets with 1 mm thickness.

Due to the size of the pores and the restrictions of the SAXS experiments, only a limited size-range can effectively be measured and evaluated. To get the full picture of size distributions, every sample would need to be evaluated with a series of different methods like transmission electron microscopy, SEM and light-optical microscopy to a significant extent to obtain statistical relevance. However, this is not necessarily useful since the retardation of grain boundary movement by pores is dependent on their size and spacing. During heat treatment, the pores may grow in size or move with the boundaries due to diffusion processes. However, after coarsening of the pores, and assuming an equal volume fraction, a wider spacing of the bubbles is apparent than in the case of small pores. Therefore, the grain boundaries are able to break away from the pinning pores [13,14].

One possible influence on pore content and their generation at elevated temperatures might be the volatilization of impurity elements. This effect is in wide-scale use for so-called non-sag W, where doping of especially K leads to the formation of gas bubbles at high temperatures. These bubbles are elongated during wire drawing and lead to linear arrays of small bubbles impeding grain boundary movement [6]. Even in technically pure Mo, as is the focus of this study, impurities are unavoidable. The contents of chemical elements remaining in the processed material are depicted in Table 1. Another method for the chemical characterization of the material and especially segregations at interfaces is atom probe tomography, which showed predominantly P, O and N at the grain boundaries of technically pure Mo [15–17]. Of special interest in the context of this work is the atom probe measurement of a presumed sinter pore by Babinsky et al. [18]. They found significant amounts of Mg, Ca, K, Al, Ba, Fe, and Si around the pore. Four of these elements have a boiling point beneath of some of the annealing temperatures used in this study.

In a simplistic approach, the amounts of volatile elements within the material were regarded as ideal gases. Modifying the fundamental ideal gas equation, as shown below, allows for an estimation of the volume fraction of pores. The pressure of the expanding volume upon reaching the respective boiling temperatures was compared to the yield strength of Mo at elevated temperature according to Eq. 2:

$$f_{VM,i} = \frac{m_i}{M_i} \bullet R \bullet T \bullet \frac{1}{\sigma_{y,T}} \bullet \rho_{Mo} \quad (2)$$

The modeled proportion of pores $f_{VM,\,i}$ is dependent on the concentration m_i and molar mass M_i of the different volatile elements. R is the ideal gas constant, T the temperature and $\sigma_{y,\,T}$ the estimated yield strength of Mo at the respective temperature. Multiplication with the density of Mo ρ_{Mo} leads to the volumetric fraction. The contribution of every element is summed up and the resulting porosity is depicted in Fig. 8 along with the high temperature yield strength of Mo and the integrated intensity Q' of samples from the three different production routes. Scattering data of the experiments with 1000 K/min heating rate were used for comparison since the experiments had been performed without variation in beam intensity. Only sample Mo2 experienced a detached thermocouple beyond 1450 °C, which does not mitigate the qualitative discussion of this model. The integrated intensities Q' are displayed as the difference to the average RT value Q'_{RT}. Ex-situ experiments are depicted in continuation of the average Q' - Q'_{RT} during the holding segment at 1500 °C. The amounts of volatile elements and their boiling or sublimation temperatures are compiled in Table 2. The concentration values are either the maximum value from Table 1 or half of the detection limit. Nitrogen is included as N_2 molecule and O was assumed to form the volatile oxide MoO_3 [19]. Only elements found within technically pure Mo as shown in literature, e.g. [15,18], were selected for this model.

The SAXS experiments cover only a limited range of the actual size

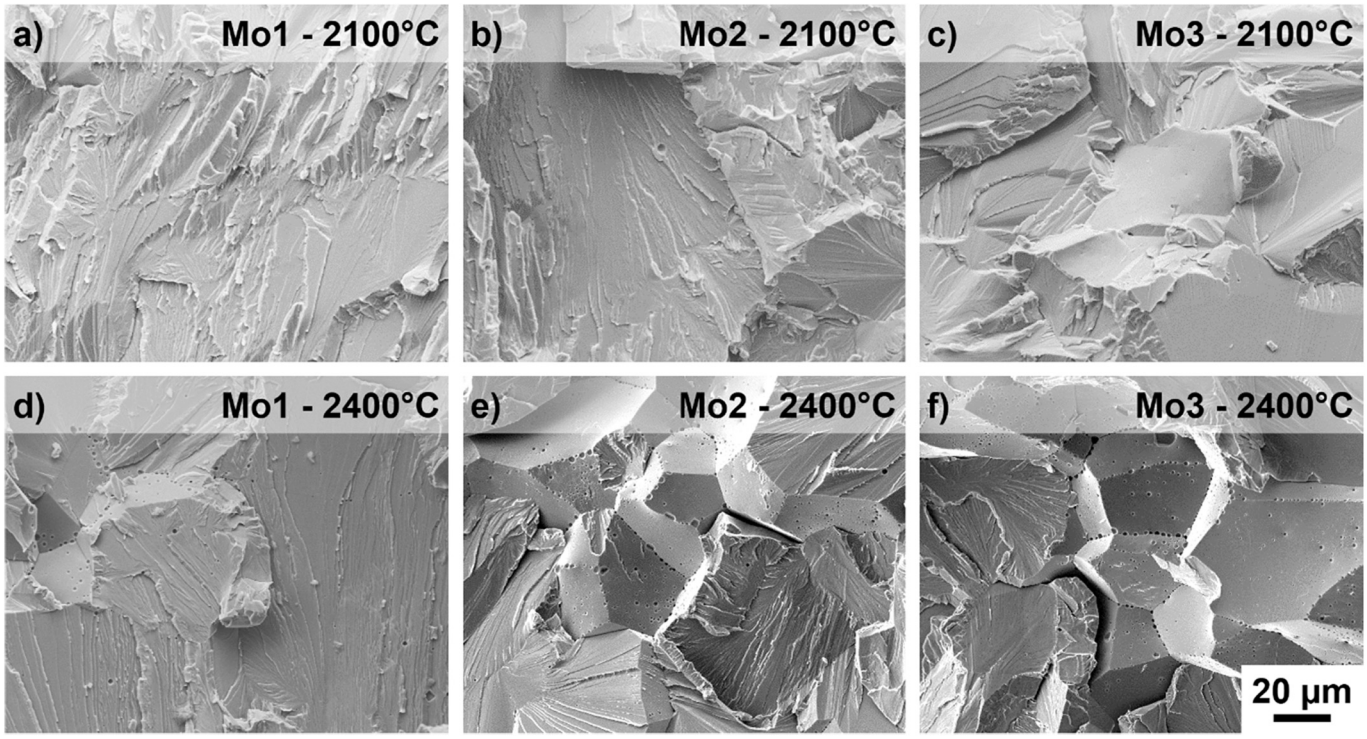

Fig. 7. Fractographs of the sheet samples annealed to 2100 °C (a to c) and 2400 °C (d to f) for 1 h in H_2 atmosphere with a heating rate of about 100 K/min. Transgranular fracture occurs for coarse-grained microstructures as can be seen, for instance, in (a). Only individual pores are visible within the grains at 2100 °C annealing temperature. At 2400 °C, a relatively high amount of porosity is visible, predominately at grain boundaries.

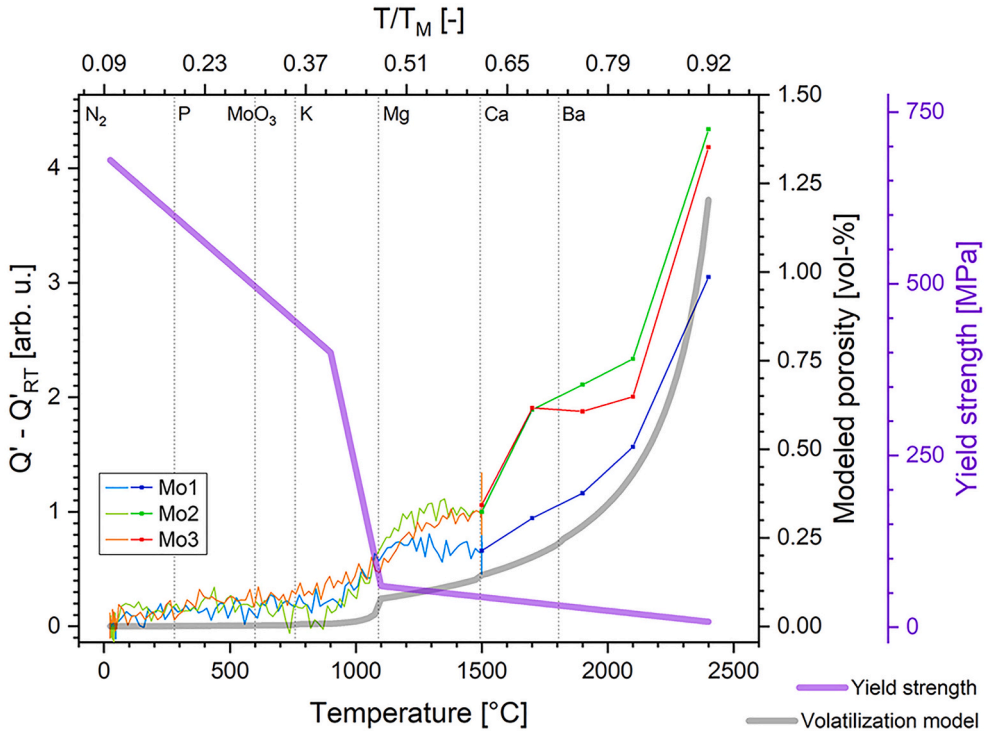

Fig. 8. Diagram of the integral intensity of the scattering experiments, estimated yield strength and modeled porosity as a function of temperature. The volatilization temperatures for different accompanying elements and compounds are depicted by dotted lines. Beside the rise in modeled porosity at the boiling point of these elements, the decreasing yield strength leads to a higher apparent volume fraction of pores. The highest values of scattering intensity as well as modeled porosity occur at the highest annealing temperature. For more details, see text.

distribution of pores. The integrated intensity Q' - Q'_{RT} offers qualitative information on the amount of pores for the measured size regime during the SAXS experiments and is suited to describe the continuation through the whole temperature range in this study. The first increase in scattering intensity at about 1100 °C is in accordance with the drop in yield strength due to primary recrystallization. Additionally, Mg becomes volatile at this temperature and causes another rise in modeled porosity. The trend to increased volume fraction during recrystallization is also present for the experiments with 1 K/min heating rate. However, it is shifted to lower temperatures of about 950 °C to 1000 °C compared to

Table 2
Concentrations and volatilization temperature of accompanying elements used in the porosity model. *…Ba content taken from [18].

Element/ compound	Concentration [µg/g]	Volatilization temperature [°C] as reported in [20]
N_2	$\frac{1}{2}\bullet 2.5$	RT
P	2	280
MoO_3	$\frac{1}{3}\bullet 12$	600
K	5	759
Mg	2.5	1090
Ca	1	1494
Ba	1.6*	1805

the experiments with a heating rate of 1000 K/min. The scattering experiments revealed a continuous increase of pores up to 2100 °C in Mo1. On the contrary, the scattering data for Mo2 and Mo3 suggest another rapid increase of scattering centers between 1500 °C and 1700 °C and moderate increase/stagnation up to 2100 °C. All samples show a distinctly higher content of pores for the highest annealing temperature of 2400 °C. The modeled porosity increases exponentially with additional contributions upon reaching the volatilization of elements.

The volatilization model does not take into account the size of pores or the surface tension. The presence and volumetric amount of pores is generalized as a trade-off between the gas pressure resulting from volatilization of certain elements and the induced thermal expansion against the resistance to plastic deformation of the material, given by the yield strength at elevated temperature. In literature, the formation of pores is described to be governed by plastic deformation in the absence of sufficient vacancy diffusion [21,22]. This is certainly the case at lower temperatures. Considering the self-diffusion of Mo with activation energies Q between 422 and 481.5 kJ/mol [23,24], one can estimate the dominance of diffusion processes by calculating a relative diffusion distance x according to Eq. 3, where D_T is the diffusion coefficient at temperature T and R the ideal gas constant.

$$x = \left(\frac{D_T}{D_{T=2400°C}}\right)^{0.5}, \text{with } D_T = D_0 \bullet exp\left\{\frac{-Q}{RT}\right\} \tag{3}$$

It becomes clear that diffusion remains insignificant ($x < 1\%$) up to about 1600 °C. Only at a considerably higher temperature of about 1900 °C ($x \sim 10\%$) diffusion starts to play a more important role.

There seems to be not much difference between the three sample variants up to the primary recrystallization at about 1100 °C during the 1000 K/min experiments. Only after this change in microstructure the observed intensity in scattering centers is increased for Mo2 and Mo3. This difference widens at 1700 °C, where Mo2 and Mo3 display an even further increase in Q' - Q'_{RT}. Both of these samples stem from the initially large sintered part and exhibit an increased O content and a slightly higher K content than Mo1 (see Table 1). Therefore, the observed increased porosity of these samples suggests that the sintering process has a more significant influence on pore formation when compared to the thermo-mechanical processing afterwards. However, regarding the different onset temperatures for secondary recrystallization (between 1700 °C and 2200 °C, see also Fig. 2), there seems to remain an influence. The samples have a different rolling history since Mo2 is machined, whereas Mo3 is primary rolled to the dimensions of Mo1 and Mo2 before the final sheet rolling. Experiments on porous copper and silver showed the influence of hot-working temperature both on pore content and retardation of primary recrystallization [8]. It is reasonable to assume that in the first rolling step of Mo3, pores are deformed to arrays of smaller pores and remain in the material. This could possibly explain the stronger impediment for grain boundary migration and therefore secondary recrystallization in Mo3.

The density measurements, as depicted in Fig. 6, show an increase in pore volume for all annealed samples. The strongest increase occurs for Mo3, which is in accordance to the relative fitted volume fractions of pores at 2400 °C. The distinctly higher amount of porosity at the highest annealing temperature of 2400 °C (corresponding to 0.92 T_M), in comparison to 2100 °C, is visible in the volume fraction during the SAXS experiments and evident from the fractographs in Fig. 7. This observation for Mo is in good agreement with investigations by Brett and Friedman on W [21]. These authors investigated the evolution of porosity in different doped and pure W samples for high homologous temperatures of 0.89 to 0.98 T_M. While the micro-sized porosity is predominantly within the grains, by contrast at the highest temperature the grain boundaries are closely covered with pores. The submicron-sized pore fraction was also evaluated by fractographs and SEM micrographs. As expected for doped W, linear arrays of fine pores are visible. However, at an annealing temperature of 3350 °C (0.98 T_M) a greater proportion of random pores appeared, also within the grains. Seemingly, this is governed by the amount and distribution of volatile impurities.

5. Conclusions and outlook

In this paper, the evolution of pores in three Mo sheet samples, fabricated from the same initial powder but using sintered parts with different starting dimensions for the rolling process, were investigated. In-situ SAXS experiments using a dilatometer were carried out, applying two different heating rates up to 1500 °C. Furthermore, ex-situ annealed samples were investigated employing annealing temperatures up to 2400 °C, corresponding to 0.92 T_M.

In a simple model, the contents and the thermal expansion of accompanying elements with volatilization temperatures below the investigated annealing temperatures were evaluated against the plastic deformation resistance of Mo at elevated temperatures. The resulting pore volume fractions were calculated, and the modeled porosity does generally match the integrated scattering intensity, confirming the validity of the simple model. The pore volume fractions suggest that the impurity elements drive pore creation and induce expansion in the material. The results further suggest an influence of the size of the sintered part: samples from a larger sintered part have slightly higher impurity content and this seems to lead to higher pore volume fractions. The observed retardation of secondary recrystallization is consistent with the obtained pore volume fractions and density measurements and can be explained by the development and presence of pores influenced by sinter format and rolling history.

The accessible minimum scattering vector was limited in this study due to the use of high-energy photons, thus limiting the maximum observable pore size. Therefore, in future research small-angle neutron scattering (SANS) would be desired to investigate larger nano-pores. Using different SANS techniques, the observable size range can be extended to the micrometer range.

CRediT authorship contribution statement

S. Jakob: Conceptualization, Formal analysis, Investigation, Methodology, Visualization, Writing – original draft. **A. Lorich:** Investigation, Validation, Writing – review & editing. **W. Knabl:** Project administration, Resources, Writing – review & editing. **A. Stark:** Investigation, Methodology. **P. Staron:** Conceptualization, Methodology, Resources, Validation, Writing – review & editing. **H. Clemens:** Conceptualization, Resources, Writing – review & editing. **P. Spoerk-Erdely:** Methodology, Validation, Writing – review & editing. **V. Maier-Kiener:** Conceptualization, Methodology, Project administration, Supervision, Writing – review & editing.

Declaration of Competing Interest

The authors declare that they have no conflict of interest.

Data availability

Data will be made available on request.

Acknowledgements

We acknowledge DESY (Hamburg, Germany), a member of the Helmholtz Association HGF, for the provision of experimental facilities at PETRA III. The beamline P07 (HEMS) is operated by Helmholtz-Zentrum Hereon and we would like to thank Norbert Schell and Emad Maawad for assistance in using the beamline and dilatometer. Beamtime was allocated for proposal I-20190886 EC.

References

[1] J.A. Shields (Ed.), Applications of Molybdenum Metal and its Alloys, 2nd ed., International Molybdenum Association (IMOA), London, UK, 2013.
[2] F.J. Humphreys, M. Hatherly, Recrystallization and Related Annealing Phenomena, 2nd ed., Elsevier, Oxford, England, 2004.
[3] O. Blaschko, G. Krexner, P. Weinzierl, U. Wien, G. Leichtfried, M. Plansee, Neutron Small-Angle Scattering Investigation on the Sintering of Molybdenum Powders, 1993, pp. 531–543.
[4] S. Primig, H. Leitner, H. Clemens, A. Lorich, W. Knabl, R. Stickler, On the recrystallization behavior of technically pure molybdenum, Int. J. Refract. Met. Hard Mater. 28 (2010) 703–708, https://doi.org/10.1016/j.ijrmhm.2010.03.006.
[5] S. Primig, H. Leitner, W. Knabl, A. Lorich, H. Clemens, R. Stickler, Influence of the heating rate on the recrystallization behavior of molybdenum, Mater. Sci. Eng. A 535 (2012) 316–324, https://doi.org/10.1016/j.msea.2011.12.099.
[6] P. Schade, 100 years of doped tungsten wire, Int. J. Refract. Met. Hard Mater. 28 (2010) 648–660, https://doi.org/10.1016/j.ijrmhm.2010.05.003.
[7] D.M. Moon, R.C. Koo, Mechanism and kinetics of bubble formation in doped tungsten, Metall. Mater. Trans. B Process Metall. Mater. Process. Sci. 2 (1971) 2115–2122, https://doi.org/10.1007/BF02917539.
[8] M.L. Bhatia, R.W. Cahn, Recrystallization of porous copper, Proc R Soc London Ser A. 362 (1978) 341–360, https://doi.org/10.1098/rspa.1978.0137.
[9] Undurchlässige Sintermetallwerkstoffe und Hartmetalle - Ermittlung der Dichte / Impermeable sintered metal materials and hardmetals - Determination of density, ICS 77.160, ISO 3369, 2022, https://doi.org/10.31030/1634435.
[10] P. Staron, T. Fischer, T. Lippmann, A. Stark, S. Daneshpour, D. Schnubel, E. Uhlmann, R. Gerstenberger, B. Camin, W. Reimers, E. Eidenberger, H. Clemens, N. Huber, A. Schreyer, In situ experiments with synchrotron high-energy X-rays and neutrons, Adv. Eng. Mater. 13 (2011) 658–663.
[11] A.P. Hammersley, S.O. Svensson, M. Hanfland, A.N. Fitch, D. Häusermann, Two-dimensional detector software: from real detector to idealised image or two-theta scan, High Pressure Res. 14 (1996) 235–248, https://doi.org/10.1080/08957959608201408.
[12] P. Staron, U. Christoph, F. Appel, H. Clemens, SANS investigation of precipitation hardening of two-phase γ-TiAl alloys, Appl. Phys. A Mater. Sci. Process. 74 (2002) 1163–1165, https://doi.org/10.1007/s003390201870.
[13] S. Friedman, J. Brett, Porosity and anomalous recrystallization behavior in doped tungsten wire, Metall. Trans. A. 1 (1970) 3225–3231, https://doi.org/10.1007/BF03038440.
[14] K. Farrell, A.C. Schaffhauser, J.T. Houston, Effect of gas bubbles on recrystallization of tungsten, Metall. Trans. A. 1 (1970) 2899–2905, https://doi.org/10.1007/BF03037829.
[15] K. Leitner (Née Babinsky), P.J. Felfer, D. Holec, J. Cairney, W. Knabl, A. Lorich, H. Clemens, S. Primig, On grain boundary segregation in molybdenum materials, Mater. Des. 135 (2017) 204–212, https://doi.org/10.1016/j.matdes.2017.09.019.
[16] K. Leitner, D. Scheiber, S. Jakob, S. Primig, H. Clemens, E. Povoden-Karadeniz, L. Romaner, How grain boundary chemistry controls the fracture mode of molybdenum, Mater. Des. 142 (2018) 36–43, https://doi.org/10.1016/j.matdes.2018.01.012.
[17] S. Jakob, A. Lorich, M. Eidenberger-Schober, W. Knabl, H. Clemens, V. Maier-Kiener, Microstructural characterization of molybdenum grain boundaries by micropillar compression testing and atom probe tomography, Pract. Metallogr. 56 (2019) 776–786, https://doi.org/10.3139/147.110567.
[18] K. Babinsky, J. Weidow, W. Knabl, A. Lorich, H. Leitner, S. Primig, Atom probe study of grain boundary segregation in technically pure molybdenum, Mater. Charact. 87 (2014) 95–103, https://doi.org/10.1016/j.matchar.2013.11.001.
[19] M. Simnad, A. Spilners, Kinetics and mechanism of the oxidation of molybdenum, J. Meteorol. 7 (1955) 1011–1016, https://doi.org/10.1007/bf03377603.
[20] N.N. Greenwood, A. Earnshaw, Chemistry of the Elements, 2nd ed, Elsevier Butterworth-Heinemann, 2012.
[21] J. Brett, S. Friedman, High temperature porosity in tungsten, Met Trans. 3 (1972) 769–778, https://doi.org/10.1007/bf02647647.
[22] G.W. Greenwood, A.J.E. Foreman, D.E. Rimmer, The role of vacancies and dislocations in the nucleation and growth of gas bubbles in irradiated fissile material, J. Nucl. Mater. 1 (1959) 305–324, https://doi.org/10.1016/0022-3115(59)90030-3.
[23] Y.V. Borisov, P.L. Gruzin, L.V. Pavlinov, G.B. Fedorov, Self-diffusion of molybdenum and diffusion of tungsten in molybdenum, Prod. Phys. Metall. Pure Met. - Transl. 1 (1959) 213–218.
[24] K. Maier, H. Mehrer, G. Rein, Self-diffusion in molybdenum, Int. J. Mater. Res. 70 (1979) 271–276.